Red perovskite light-emitting diodes with efficiency exceeding 25% realized by cospacer cations

Ji Jiang
Institute of Semiconductors, CAS https://orcid.org/0000-0002-7536-7507
Zema Chu
Institute of Semiconductors, CAS
Zhigang Yin
Institute of Semiconductors, Chinese Academy of Sciences
Jingzhen Li
Institute of Semiconductors, CAS
Yingguo Yang
Shanghai Institute of Applied Physics https://orcid.org/0000-0002-1749-2799
Jingren Chen
Institute of Semiconductors, CAS
Jinliang Wu
Institute of Semiconductors, Chinese Academy of Sciences
Jingbi You
Institute of Semiconductors https://orcid.org/0000-0002-4651-9081
Xingwang Zhang (xwzhang@semi.ac.cn)
Institute of Semiconductors, CAS https://orcid.org/0000-0001-7873-5566

Article

Keywords:

Posted Date: March 24th, 2022

DOI: https://doi.org/10.21203/rs.3.rs-1417650/v1

Abstract

Perovskite light-emitting diodes (PeLEDs) own great attention in recent years, due to their narrow emission bandwidth and tunable emission spectrum. Efficient red emission is one of most important part for lighting and display. Quasi-two-dimensional (quasi-2D) perovskite could deliver high emission efficiency due to the strong carrier confinement, while the external quantum efficiencies (EQE) of red quasi-2D PeLEDs are inefficient at present, which is due to the complex distribution of different n-value phases in quasi-2D perovskite films. Here, we finely control the phase distribution of the quasi-2D perovskite by mixing two different large organic cations, which effectively reduce the amount of smaller n index phases, meanwhile the passivation of lead and halide defects in perovskite films is realized. Accordingly, the PeLEDs showed 25.8% EQE and 1300 cd•m-2 maximum brightness at 680 nm, which exhibit the highest performance for red PeLEDs up to now.

Full Text

Solution-processed metal halide perovskites have attracted considerable research interest as a new type of semiconductor materials, which has been utilized in solar cells, light-emitting diodes and other optoelectronic devices [1-8]. In particular, Perovskite light-emitting diodes (PeLEDs) have been conferred as the cutting-edging research due to their high performance [9-16], red emission is very important in the field of lighting and display. To date, the red PeLEDs have achieved significant external quantum efficiencies (EQE) that over 20%, most of them are based on the three-dimensional (3D) and quantum-dot (QD) perovskite material [17-22].

Compared with 3D and QD perovskite, quasi-two-dimensional (quasi-2D) perovskite could be more efficient emission material due to its higher exciton binding energy, multi-quantum-well structure and good charge transfer properties [23-28]. Ruddlesden-Popper perovskite (RPP) is generally described by the formula of $L_2A_{n-1}B_nX_{3n+1}$ as typical quasi-2D perovskites, which consist of large organic cation L, a small organic or cesium cation A, divalent metal cation B (lead or tin), and halide anion X (Cl^-, Br^- or I^-). Although the overall development of red LED is remarkable, the quasi-2D red LEDs are still in arrears of efficiency. The reason may be that fine control of quasi-2D perovskite phase (represents the thickness of the $[PbI_6]^{4-}$ octahedra layers capped by the L cations [28-31]) distribution is a great challenge, which make the inferior charge injection and serious non-radiative recombination.

In this work, we report a general strategy of cospacer cations to control the phase distribution in RPP films, by mixing a representative of phenethylammonium iodide (PEAI)/ 3-fluorophenylethylammonium iodide (m-F-PEA) and 1-naphthylmethylammonium iodide (NMAI) to alloy the RPP films. These RPP films show significant suppression of small index phase (n=2), and the carrier transport has been improved effectively. At the same time, the mixing of NMA can reduce the metallic Pb states and halide defects in RPP films, moreover, a smooth and pinhole-free perovskite film has been obtained. As a result, larger than 90% photoluminescence quantum yield (PLQY) is achieved through the mixing of m-F-PEA and NMA with

a mixing ratio of 6:4, the LED prepared by this method achieves the efficiency as high as 25.8% and the maximum luminance of exceeding 1300 cd•cm^{-2} at 680 nm.

We prepared RPP films of $(PEA_xNMA_{1-x})_2CsPb_2I_7$ and $(m\text{-}F\text{-}PEA_xNMA_{1-x})_2CsPb_2I_7$ with different composition (x = 0, 0.2, 0.4, 0.6, 0.8 and 1) to study the effect of cospacer cations on perovskite properties. The molecular structures of PEA, m-F-PEA and NMA cations are shown in Fig. 1a, m-F-PEA represents that a halide F atom is contained on the para-position on the conjugated phenyl ring in PEA. Among them, we found that the mixed cation perovskite with x=0.6 is the optimized condition, which will be shown in the following. PEA cation only and cation mixture perovskites are expressed as P10N0, P6N4 and mFP6N4 in this study, here P means PEA, mFP means m-F-PEA, and N refers to NMA. Fig. 1b represents ultraviolet-visible (UV-Vis) absorption spectra and steady photoluminescence (PL) spectra of the three films. The multiple absorption peaks suggest that thin perovskite films likely contain mixed quasi-2D structures with different n values [32-33]. The film P10N0 shows several strong exciton absorption peaks at ~560 nm and ~610 nm, corresponding to the phase of n = 2 and 3. While introducing NMA, the films of P6N4 and mFP6N4 absorption peaks corresponding to n = 2 and 3 are decreased significantly, and the peak of n = 2 is almost negligible in the mFP6N4 film. Consisting with the absorption, the film P10N0 shows obvious emission peaks of n = 2 and 3. And the films P6N4 and mFP6N4 mainly contain large n phase, which lead to the red-shifted PL spectra and no obvious emission of n = 2. The comprehensive UV–vis absorption spectra and PL spectra from quasi-2D perovskite films with different compositions (Supplementary Fig. 1, 2) confirm this trend. It must be noted, along with the red-shift of PL for cospacer cations, the full width at half maximum (FWHM) decreased from 43 nm to 34 nm, indicating that the phase distribution in quasi-2D perovskite become narrow. The weak PL intensity of P10N0 and P0N10 samples could due to the trap-assisted nonradiative recombination and strong electron–phonon coupling [34-36]. We carried out PLQY measurements for these three films, as seen from Fig. 1c, the PLQY of perovskite sample increases from 53% (P10N0) to 78% (P6N4) and 91% (mFP6N4) while using cospacer cations, and the targeted films exhibit strong emission under ultraviolet illumination (Supplementary Fig. 3). Fig. 1d shows the time-resolved photoluminescence (TRPL) decay profiles of different samples, with the mixing of NMA, the average PL lifetime of the quasi-2D film gradually increases from 5.321 ns (P10N0) to 8.308 ns (P6N4) and 8.523 ns (mFP6N4), suggesting the suppression of nonradiative recombination while engineering cations.

Fig. 2a represents the X-ray diffraction (XRD) patterns of different quasi-2D perovskite films, the strong diffraction peak of n = 2 ($2\theta = 3.8°$) can be observed in P10N0 film, indicating a dominant of small index of n = 2 phase. As NMA mixed with PEA/ m-F-PEA, the peaks of n = 2 phase reduce significantly, and the large-n phases become the main part in the P6N4 and mFP6N4 films. Compared with the (212) and (111) peaks in P10N0 film, the strong (110) and (220) peaks are observed from P6N4 and mFP6N4 films, implying that the preferred orientation has been formed in the cospacer cation perovskite. In addition, grazing-incidence wide-angle X-ray scattering (GIWAXS) measurements were performed to further investigate the crystal phase and crystallinity of the quasi-2D films, the Debye-Scherrer rings showed in P10N0 films indicate a random crystalline orientation, while stronger scattering spots along the q_z

direction are exhibited in P6N4 and mFP6N4 indicating a vertical alignment of (110) with respect to the substrate (Fig. 2b-d), which facilitates the charge vertical transport [37-39]. The crystallinity of perovskite with different crystal planes collected by high-resolution transmission electron microscopy (HRTEM) is shown in Fig. 2e-f. For the P10N0 film, the n = 2 phase crystal planes in P10N0 can be clearly observed, the crystal plane of (212) and (111) from large n phase (close to 3D perovskite) are also found in Supplementary Fig. 4. While for the cospacer cation films, the dominant (110) crystal plane with good crystallization were observed, consistent with our finding in the XRD results.

Time-resolved transient absorption (TA) measurements were carried out to derive the phase distribution and energy funnel process in quasi-2D perovskite films. For the P10N0 film, as seen from Fig. 3a, d, there are several ground-state bleaching (GSB) peaks around 560, 610, 635, 655 and 670 nm, which correspond to the phase of n = 2, 3, 4, 5, and n ≥ 6 in RPP film and represent the evolution of excited-states carriers, respectively.

And it can also be found that the photogenerated carriers are initially formed in the wide-bandgap quantum well of n = 2 phase, while the charge transfer process from n = 2 phase to large-n phase is more than 100 ps based on the absorption bleaching results, which could retard carrier concentration and reduce radiative recombination in the emitting center (large-n phases) [29]. For the cospacer cation films, as shown in Fig. 3b, e and c, f, the peaks of different phases still exist, the most significant difference is that the peak of n = 2 phase is almost negligible after attenuation of about 1 ps, indicating much faster charge transfer happened in the quantum well structure for the cospacer cation system.

To further study the energy transfer process, the kinetics of each GSB are fitted by a function that includes a fast decay component τ_1 related to the carrier transferring from small-n phase to large-n phases in perovskite film, slow decay components τ_2 and τ_3 related to the energy decay and recombination, and the rapid increase component τ_{et} related to the establishment of GSB peak [40-41], Fig. 3g-i show the decay kinetics about different phases of three perovskite films, the results of fitted lifetime components are given in Supplementary Table 1. The fast decay time τ_1 of n = 2 and n = 3 phases in P10N0 film are 0.44 and 0.19 ps, respectively, then the excitons continuously transferred to n ≥ 6 phases for the radiative recombination. Encouragingly, the fast decay time τ_1 of n = 2 phase in P6N4 (0.05 ps) and mFP6N4 (0.05 ps) are 9 times shorter than that in the pristine one, with τ_1 of n = 3 phase in P6N4 (0.10 ps) and mFP6N4 (0.10 ps), which are 2 times shorter than that in P10N0. The shorter τ_1 means that the carriers are transferred out of the quantum well at a faster rate [25]. Meanwhile, the establishment time τ_{et} of the emission phase for P10N0, P6N4, and mFP6N4 is 1.21 ps, 1.10 ps, and 1.02 ps, respectively. The above results show that the cospacer cation strategy can effectively improve the energy transfer process in the perovskite films.

X-ray photoelectron spectroscopy (XPS) measurements were performed to check the effect of the cospacer cations on the chemical states of the elements in the perovskite. The core levels of Pb $4f_{7/2}$ from the three different compositions of perovskite are shown in Fig. 3a-c. The dominant peak around

138 eV is corresponding to the Pb-I bond in $[PbI_6]^{4-}$, and the shoulder peak around 136 eV corresponds to metallic Pb states. For the control film, an obvious Pb metallic state can be easily found, which is detrimental to the PeLED performance due to the serious non-radiative recombination [3]. After mixing the PEA with NMA, the metallic Pb peak becomes weak but still exist, and it is very encouraging that the metallic Pb peak is fully suppressed in mFP6N4 system. The reduction of metallic Pb states could be one of main reasons for the high PLQY for the cospacer cation system.

In addition to the suppression of metallic Pb states, we also found that there are some chemical shifts for the I core level. Compared with P10N0 and P6N4, the core level of I in mFP6N4 exhibits a blue-shift of 0.2 eV (Supplementary Fig. 5), means the stronger interaction between I and Pb and a more stable crystal structure [42-43]. The main effect could be due to the substitution of fluorine for hydrogen on the benzene ring of PEA, which will change the electronic structure of the molecule, then resulting slight differences in octahedral tilting, shorter average phenyl ring centroid-centroid distances and more tightly stacked perovskite sheets [42-45]. Meanwhile, the electron withdrawing of F atom could suppress the formation of halide dangling bonds [21].

Scanning electron microscopy (SEM) was used to investigate the surface morphology of thin quasi-2D perovskite films, as shown in Fig.4d-f. It is noticeable that the P10N0 perovskite film shows obvious pinholes and isolated large grains, which could be detrimental to achieving high device performance due to the current leakage. We found that the cospacer cations could effectively reduce the pinhole and suppress the formation of large isolated particles, and it is very encouraging that the perovskite film becomes very dense and continuous while mixing m-F-PEA and NMA. In previous studies, it has been reported that low-dimensional perovskite tends to aggravate the formation of larger grains and rougher perovskite films, due to the existence of layer perovskite phases [40-41]. This study has confirmed that the strategy of cospacer cations can reduce the small index of quasi-2D perovskite, which guarantees the formation of smaller grains and reduces the surface holes and defects of perovskite. Atomic force microscopy (AFM) results also confirmed the better morphology while mixing m-F-PEA with NMA (Supplementary Fig. 6), the root mean square roughness of three perovskite films decreased from 2.89 nm (P10N0) to 2.12 nm (P6N4) and 1.74 nm (mFP6N4).

We fabricate the perovskite films into configure LEDs based on device structure of ITO/ the modified PEDOT: PSS (m-PEDOT: PSS) (40 nm)/ poly-TPD (Poly(N, N'-bis(4-butylphenyl)-N,N'-bis(phenyl)-benzidine)) (10 nm)/ PVK (poly(9-vinlycarbazole)) (5 nm) / quasi-2D perovskite (30 nm)/ TPBi (2,2',2"-(1,3,5-benzinetriyl)-tris(1-phenyl-1H-benzi-midazole)) (30 nm)/ LiF (1 nm) Al (100 nm). Fig. 5a shows a schematic of the flat-band energy-level diagram of the multiple layers. The cross-sectional SEM image of devices is shown in Fig. 5b, and a clear sandwich structure is clearly observed. The typical electroluminescence (EL) spectra of P10N0, P6N4 and mFP6N4 are shown in Fig. 5c. Although the quasi-2D perovskite films exhibit a mixture of many phases with different bandgaps, only a single red EL peak is observed. Compared with the peak of P10N0 (~660 nm), the peaks of P6N4 and mFP6N4 (~680 nm) have a slight red-shift, which is consistent with the PL results (Fig. 1a).

According to the current density–voltage–luminance (J-V-L) plot (Fig. 5d), the leakage current of the P10N0 film is obviously higher than that of films with cospacer cations, but the subsequent injection current is lower, indicating that there is a higher defect density in P10N0 films and the redundant n = 2 phase will hinder the injection of current [46]. Furthermore, it could be found that the leakage current of P6N4 is slightly higher than that of mFP6N4, which consists with that mFP6N4 owns better morphology. In Fig. 5e, it is apparent that the performance of the devices with cospacer cations is better than that of the device with single organic cation, a very high EQE value of 24.2% is achieved with a luminance of 1300 cd•m^{-2} in mFP6N4 film, while just 20.6% with 850 cd•m^{-2} in P6N4 and 12.7% with 500 cd•m^{-2} in P10N0, and the maximum EQE of champion PeLED based on mFP6N4 could reach 25.8% (Fig. 5f). The EL spectrum of the device under different voltages is given in Supplementary Fig. 7. As the bias voltage increases, the device shows good spectral stability and also with nice EL performance at Commission Internationale de l'Eclairage (CIE) coordinates of (0.722, 0.277) (Supplementary Fig. 8). We also collected the EQE data for 27 devices, the device shows only 5.1% relative deviation (Supplementary Fig. 9), demonstrating the good reproducibility of the cospacer cation strategy. In addition to increase the device efficiency, we also found that the cospacer cation method improves the operational stability, the T_{50} operational time was increased to over 5 times with an initial brightness of 100 cd•m^{-2} (Supplementary Fig. 10), which could be due to the passivation of the defects in the perovskite layer (Fig. 3a-c) and also the increase of the chemical bonding (Supplementary Fig. 5).

In conclusion, cospacer cation quasi-2D $(PEA/m\text{-}F\text{-}PEA)_xNMA_{1-x})_2CsPb_2I_7$ RPP films were developed for efficient red PeLED. Low-dimensional with small index (n = 2) perovskite phase is suppressed by cospacer cation modulation, which is helpful for charge transfer. Meanwhile, the metallic Pb states and halide defects in perovskite films are passivated. Accordingly, efficient red PeLED with a maximum EQE of 25.8% at 680 nm is achieved. Our method provides an efficient strategy to control phase distribution and passivate defects simultaneously, which is beneficial to realize more efficient PeLEDs and could also be good for solar cells.

Experimental Section

Materials: CsI, PbI_2, LiF, dimethyl sulfoxide (DMSO), ethyl acetate (EA), chlorobenzene and poly (sodium 4-styrenesulfonate) (PSS-Na, average Mw ~ 70000) were purchased from Sigma-Aldrich. TPBi, PEAI, m-F-PEA, NMAI and PVK (average Mw >100000) were purchased from Xi'an Polymer Technology Corp. Poly-TPD was purchased from 1-Material. And the m-PEDOT: PSS solution was a mixture of normal PEDOT: PSS (AI 4083) aqueous solution with 100 mg•ml^{-1} PSS-Na aqueous solution by a volume ratio of 6: 5.

Perovskite Precursor Synthesized: The quasi-2D perovskite $(PEA)_2CsPb_2I_7$ precursor was prepared by dissolving PEAI, CsI, and PbI_2 in a molar ratio of 1:0.75:1 in DMSO under continuous stirring overnight at 40 °C, keeping the molar concentration Pb^{2+} at 0.5 M. And $((PEA/m\text{-}F\text{-}PEA)_xNMA_{1-x})_2CsPb_2I_7$ precursor was prepared by mixing PEA/m-F-PEA and NMA in a molar ratio of *x*: 1-*x* on the basis of single-cation perovskite (*x* = 0, 0.2, 0.4, 0.6, 0.8 and 1).

Device Fabrication: Indium tin oxide (ITO)-coated glass substrates were sequentially cleaned in detergent, deionized water, acetone, isopropyl alcohol. Then dry it with nitrogen and treat it with ultraviolet ozone for 20 minutes. The m-PEDOT: PSS aqueous solution was spin-coated at 7000 rpm for 40 s, followed by drying at 160 °C for 15 min in ambient air. Then, the samples were transferred into a nitrogen-filled glovebox, spin-coating poly-TPD (10 mg/ml in chlorobenzene) and PVK (2.5 mg/ml in chlorobenzene) on the m-PEDOT: PSS substrate at 2000 rpm for 40 s in turn, and annealing at 150 °C for 30 min. The RPP films were fabricated by spin-coating the precursor solutions at 9000 rpm for 60 s, and after spin-coating for 15 s, 120 μL of EA was poured onto the film as an anti-solvent, followed by annealing at 80 °C for 15 min. Finally, the TBPi layer (30 nm) and LiF/ Al electrodes (1 nm/100 nm) were deposited through a shadow mask in a high vacuum of ~ 1×10^{-4} Pa thermal evaporator. The device active area was 0.1 cm^2 as defined by the overlapping area of the ITO and Al electrode.

Film and Device Characterization Measurement: Absorption spectra were measured using a UV–vis spectrometer (Cary 5000). PL spectra and TRPL were acquired at room temperature in the ambient air using a FLS1000 spectrometer with excitation at 375 nm from a 450 W Xenon lamp and the estimated light power density incident on the samples was about 3.5 $mW\bullet cm^{-2}$. PLQYs of the perovskite thin films were recorded by a commercialized PLQY measurement system (LQE-50-PL) from Enlitech with excitation from a 368 nm LED. The XRD patterns of the perovskite thin films were performed with a Rigaku D/max 2500H equipment with a conventional Cu target X-ray tube (Cu K-alpha, λ = 1.5405 Å), with X-ray generator settings at 40 kV and 30 mA. The GIWAXS was performed at BL17B1 beamline of SSRF using the X-ray energy of 10KeV. Two-dimensional patterns were acquired by a PLATUS 2M detector mounted vertically at a distance ~240 mm from the sample with a grazing incidence angle of 0.2º or 0.4 º and an exposure time of 20 sec. The TA measurement was carried out by a homebuilt spectroscopy setup, with the laser source of a commercial femtosecond amplifier laser system (70 fs, 2 kHz, 800 nm, Solstice, Spectra Physics) and the collection device of a laser frequency synchronized fiber optical spectrometer (AvaSpec-ULS2048CL-EVO, Avantes). The output pulse was split into two beams. The first beam was used to pump a commercial optical parametric amplifier (TOPAS prime, Spectra Physics) and frequency converter to provide a frequency tunable femtosecond laser source. The second beam with weaker energy was focused into a CaF_2 plate (4 mm thickness) to generate a white light continuum as the probe. During the experiment, UV femtosecond laser pulses centered at 340nm was used and the pump intensity was set to be 12 $uJ\bullet cm^{-2}$. XPS was performed on ESCALab 250Xi of Thermo Scientific using 200 W monochromated al Kα (1486.6 eV) radiation and adopting 500 μm X-ray spot to analyze XPS while the analysis chamber bottom pressure ~ 3×10^{-10} mbar. Typically, the hydrocarbon C 1s line is formed from amorphous carbon at 284.8 eV for reference energy. AFM measurements were carried out by a Bruker FASTSCANBIO in non-contact mode. The SEM images were carried out by a field-emission SEM (FEI NanoSEM650), which used an electron beam accelerated at 500 V to 30 kV. TEM was carried out with a JEOL JEM-2100F, operated at 200 kV.

The EQE, I-V-L curve, EL spectrum, CIE, and operating lifetime of the perovskite LED were carried out simultaneously by a commercialized system (LQE-50-EL, Enlitech) with an integrated sphere and

photomultiplier tubes (PTM), which is used to measure the low luminance, and all electrical tests are conducted at room temperature in the ambient air for the un-encapsulated devices.

Declarations

Acknowledgements:

This work was financially supported by the Strategic Priority Research Program of Chinese Academy of Sciences (XDB43000000) and also by the National Natural Science Foundation of China (Grant Numbers: 61925405).

Author contributions

J. J., J. Y. and X. Z. initiated and designed the study. J. Y. and X. Z. supervised the work. J. J. performed experiments and analyzed data. Z. C. and J. L. helped to analyze the data. Y. Y. measured and analyzed GIWAX. All authors contributed to discussions and finalizing the manuscript. The authors declare no competing interests.

References

1. Min, H. <iuvertical-align:super;>et</iuvertical-align:super;> *al.* Perovskite solar cells with atomically coherent interlayers on SnO_2 electrodes. Nature **598**, 444–450 (2021).
2. Deschler, F. <iuvertical-align:super;>et</iuvertical-align:super;> *al.* High photoluminescence efficiency and optically pumped lasing in solution-processed mixed halide perovskite semiconductors. J. Phys. Chem. Lett. **5**, 1421–1426 (2014).
3. Cho, H. <iuvertical-align:super;>et</iuvertical-align:super;> *al.* Overcoming the electroluminescence efficiency limitations of perovskite light-emitting diodes. Science **350**, 1222–1225 (2015).
4. Sutherland, B. R., *et al.* Perovskite photonic sources. Nat. Photonics **10**, 295–302 (2016).
5. Kuang, C. <iuvertical-align:super;>et</iuvertical-align:super;> *al.* Critical role of additive-induced molecular interaction on the operational stability of perovskite light-emitting diodes. Joule **5**, 618–630 (2021).
6. Lee, H., *et al.* Perovskite emitters as a platform material for down-conversion applications. Adv. Mater. Technol. **5**, 2000091 (2020).
7. Kim, Y. -H. <iuvertical-align:super;>et</iuvertical-align:super;> *al.* Comprehensive defect suppression in perovskite nanocrystals for high-efficiency light-emitting diodes. Nat. Photonics **15**, 148–155 (2021).
8. Chu, Z. <iuvertical-align:super;>et</iuvertical-align:super;> *al.* Perovskite light-emitting diodes with external quantum efficiency exceeding 22% *via* small-molecule passivation. Adv. Mater. **33**, 2007169 (2021).

9. Byun, J. <iuvertical-align:super;>et</iuvertical-align:super;> *al.* Efficient visible quasi-2D perovskite light-emitting diodes. Adv. Mater. **28**, 7515–7520 (2016).
10. Vashishtha, P. <iuvertical-align:super;>et</iuvertical-align:super;> *al.* High efficiency blue and green light-emitting diodes using Ruddlesden-Popper inorganic mixed halide perovskites with butylammonium interlayers. Chem. Mater. **31**, 83–89 (2019).
11. Ma, D. <iuvertical-align:super;>et</iuvertical-align:super;> *al.* Distribution control enables efficient reduced-dimensional perovskite LEDs. Nature **599**, 594–598 (2021).
12. D'innocenzo, V. <iuvertical-align:super;>et</iuvertical-align:super;> *al.* Excitons versus free charges in organo-lead tri-halide perovskites. Nat. Commun. **5**, 1–6 (2014).
13. Gedda, M. <iuvertical-align:super;>et</iuvertical-align:super;> *al.* Ruddlesden-Popper-phase hybrid halide perovskite/small-molecule organic blend memory transistors. Adv. Mater. **33**, 2003137 (2021).
14. Lin, K. <iuvertical-align:super;>et</iuvertical-align:super;> *al.* Perovskite light-emitting diodes with external quantum efficiency exceeding 20 per cent. Nature **562**, 245–248 (2018).
15. Tan, Z. -K. <iuvertical-align:super;>et</iuvertical-align:super;> *al.* Bright light-emitting diodes based on organometal halide perovskite. Nat. Nanotechnol. **9**, 687–692 (2014).
16. Abdi-Jalebi, M. <iuvertical-align:super;>et</iuvertical-align:super;> *al.* Maximizing and stabilizing luminescence from halide perovskites with potassium passivation. Nature **555**, 497–501 (2018).
17. Zhu, L. <iuvertical-align:super;>et</iuvertical-align:super;> *al.* Unveiling the additive-assisted oriented growth of perovskite crystallite for high performance light-emitting diodes. Nat. Commun. **12**, 5081 (2021).
18. Cao, Y. <iuvertical-align:super;>et</iuvertical-align:super;> *al.* Perovskite light-emitting diodes based on spontaneously formed submicrometre-scale structures. Nature **562**, 249–253 (2018).
19. Chiba, T. <iuvertical-align:super;>et</iuvertical-align:super;> *al*. Anion-exchange red perovskite quantum dots with ammonium iodine salts for highly efficient light-emitting devices. Nat. Photonics **12**, 681–687 (2018).
20. Wang, Y. <iuvertical-align:super;>et</iuvertical-align:super;> *al.* All-inorganic quantum-dot LEDs based on a phase-stabilized alpha-CsPbI3 perovskite. Angew. Chem. Int. Ed. Engl. **60**, 16164–16170 (2021).
21. Fang, Z. <iuvertical-align:super;>et</iuvertical-align:super;> *al*. Dual passivation of perovskite defects for light-emitting diodes with external quantum efficiency exceeding 20%. Adv. Funct. Mater. **30**, 1909754 (2020).
22. Lee, T. *et al*. Bright and stable quantum dot light-emitting diodes. Adv. Mater. 34, 2106276 (2022).
23. Zhao, B. <iuvertical-align:super;>et</iuvertical-align:super;> *al.* Efficient light-emitting diodes from mixed-dimensional perovskites on a fluoride interface. Nat. Electron **3**, 704–710 (2020).
24. Qing, J. <iuvertical-align:super;>et</iuvertical-align:super;> *al.* Spacer cation alloying in Ruddlesden-Popper perovskites for efficient red light-emitting diodes with precisely tunable wavelengths. Adv. Mater. **33**, 2104381 (2021).

25. Wang, N. <iuvertical-align:super;>et</iuvertical-align:super;> *al.* Perovskite light-emitting diodes based on solution-processed self-organized multiple quantum wells. Nat. Photonics **10**, 699–704 (2016).
26. Yang, X. <iuvertical-align:super;>et</iuvertical-align:super;> *al.* Efficient green light-emitting diodes based on quasi-two-dimensional composition and phase engineered perovskite with surface passivation. Nat. Commun. **9**, 570 (2018).
27. Chu, Z. <iuvertical-align:super;>et</iuvertical-align:super;> *al.* Large cation ethylammonium incorporated perovskite for efficient and spectra stable blue light-emitting diodes. Nat. Commun. 11, 4165 (2020).
28. Chen, W. *et al.* Polymerized hybrid perovskites with enhanced stability, flexibility, and lattice rigidity. Adv. Mater. **33**, 2104842 (2021).
29. Kim, H. <iuvertical-align:super;>et</iuvertical-align:super;> *al.* Proton-transfer-induced 3D/2D hybrid perovskites suppress ion migration and reduce luminance overshoot. Nat. Commun. **11**, 3378 (2020).
30. Pang, P. <iuvertical-align:super;>et</iuvertical-align:super;> *al.* Rearranging low-dimensional phase distribution of quasi-2D perovskites for efficient sky-blue perovskite light-emitting diodes. ACS Nano **14**, 11420–11430 (2020).
31. Stoumpos, C. C. <iuvertical-align:super;>et</iuvertical-align:super;> *al.* Ruddlesden-Popper hybrid lead iodide perovskite 2D homologous semiconductors. Chem. Mater. **28**, 2852–2867 (2016).
32. Blancon, J. C. <iuvertical-align:super;>et</iuvertical-align:super;> *al.* Extremely efficient internal exciton dissociation through edge states in layered 2D perovskites. Science **355**, 1288–1291 (2017).
33. Liang, C. <iuvertical-align:super;>et</iuvertical-align:super;> *al.* Two-dimensional Ruddlesden-Popper layered perovskite solar cells based on phase-pure thin films. *Nat. Energy*<iuvertical-align:super;></iuvertical-align:super;>**6**, 38–45 (2021).
34. Yang, L. <iuvertical-align:super;>et</iuvertical-align:super;> *al.* Pure red light-emitting diodes based on quantum confined quasi-two-dimensional perovskites with cospacer cations. ACS Energy Letters **6**, 2386–2394 (2021).
35. Price, C. C. <iuvertical-align:super;>et</iuvertical-align:super;> *al.* Interfacial electromechanics predicts phase behavior of 2D hybrid halide perovskites. ACS Nano **14**, 3353–3364 (2020).
36. Gong, X. <iuvertical-align:super;>et</iuvertical-align:super;> *al.* Electron-phonon interaction in efficient perovskite blue emitters. Nat. Mater. **17**, 550–556 (2018).
37. Guo, Z. <iuvertical-align:super;>et</iuvertical-align:super;> *al.* Promoting energy transfer via manipulation of crystallization kinetics of quasi-2D perovskites for efficient green light-emitting diodes. Adv. Mater. **33**, 2102246 (2021).
38. Liang, D. <iuvertical-align:super;>et</iuvertical-align:super;> *al.* Unveiling crystal orientation in quasi-2D perovskite films by in situ GIWAXS for high-performance photovoltaics. *Small* **17**, 2100972 (2021).
39. Zhang, H. <iuvertical-align:super;>et</iuvertical-align:super;> *al.* Bottom-up quasi-epitaxial growth of hybrid perovskite from solution process-achieving high-efficiency solar cells via template -guided crystallization. Adv. Mater. **33**, 2100009 (2021).

40. Xu, L. <iuvertical-align:super;>et</iuvertical-align:super;> *al.* A bilateral interfacial passivation strategy promoting efficiency and stability of perovskite quantum dot light-emitting diodes. Nat. Commun. **11**, 3902 (2020).
41. Meng, F. <iuvertical-align:super;>et</iuvertical-align:super;> *al.* Co-interlayer engineering toward efficient green quasi-two-dimensional perovskite light-emitting diodes. Adv. Funct. Mater. **30**, 1910167 (2020).
42. Xie, H. <iuvertical-align:super;>et</iuvertical-align:super;> *al.* Effects of precursor ratios and annealing on electronic structure and surface composition of CH3NH3PbI3 perovskite films. J. Phys. Chem. C **120**, 215–220 (2016).
43. Wang, H. et al. Trifluoroacetate induced small-grained CsPbBr3 perovskite films result in efficient and stable light-emitting devices. Nat. Commun. **10**, 665 (2019).
44. Hu, J. <iuvertical-align:super;>et</iuvertical-align:super;> *al.* Synthetic control over orientational degeneracy of spacer cations enhances solar cell efficiency in two-dimensional perovskites. Nat. Commun. **10**, 1276 (2019).
45. Zhang, F. <iuvertical-align:super;>et</iuvertical-align:super;> *al.* Enhanced charge transport in 2D perovskites via fluorination of organic cation. J. Am. Chem. Soc. **141**, 5972–5979 (2019).
46. Liu, Z. <iuvertical-align:super;>et</iuvertical-align:super;> *al.* Perovskite light-emitting diodes with EQE exceeding 28% through a synergetic dual-additive strategy for defect passivation and nanostructure regulation. Adv. Mater. **33**, 2103268 (2021).

Figures

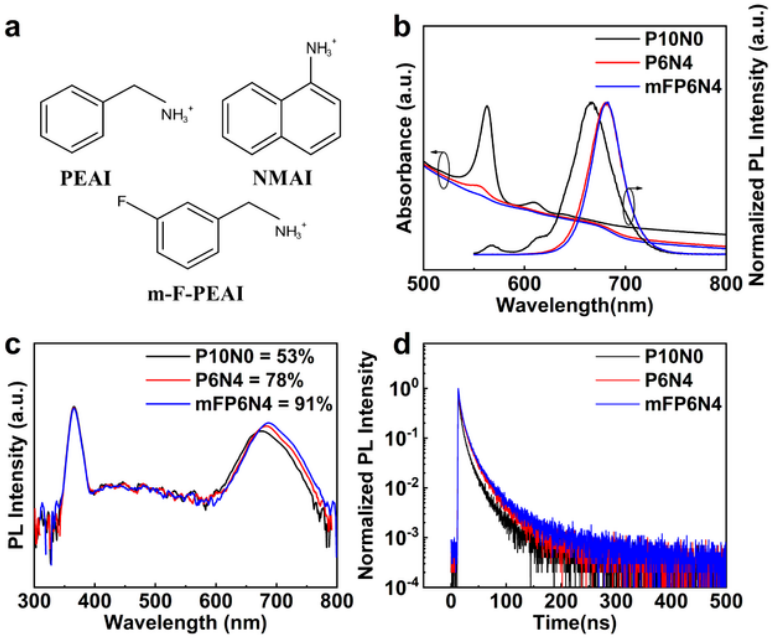

Figure 1

Characteristics of quasi-2D perovskites with different compositions. a, Molecular structure of PEA, m-F-PEA and NMA. **b**, ultraviolet-visible (UV-Vis) absorption spectra and photoluminescence (PL) spectra of P10N0, P6N4 and mFP6N4. **c**, Photoluminescence quantum yield (PLQY) of P10N0, P6N4 and mFP6N4. **d**, Time resolved photoluminescence (TRPL) of P10N0, P6N4 and mFP6N4.

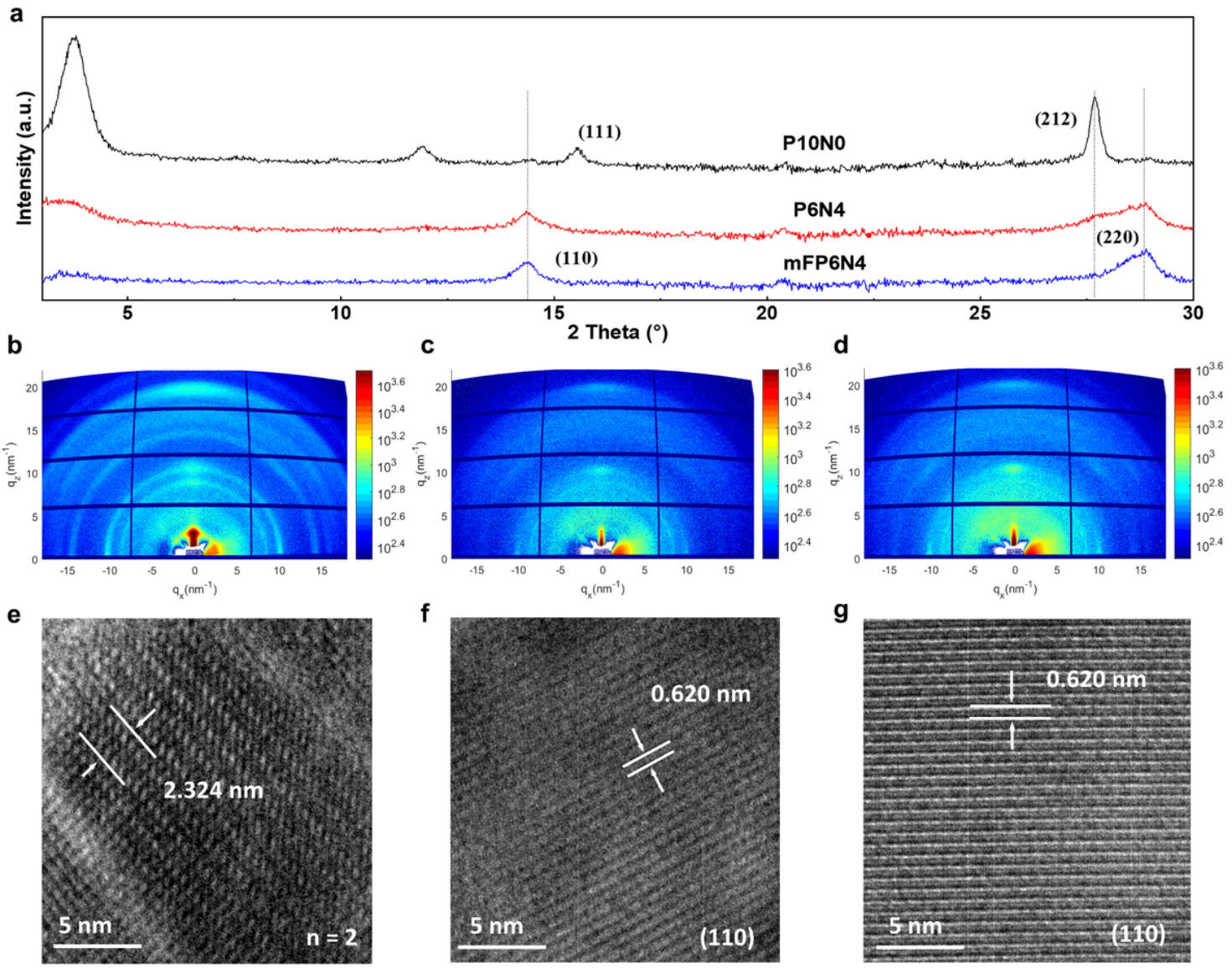

Figure 2

Microstructure of quasi-2D films with different compositions. a, X-ray diffraction (XRD) pattern of P10N0, P6N4 and mFP6N4. **b-d**, GIWAXS maps of (**b**) P10N0, (**c**) P6N4 and (**d**) mFP6N4. **e-g**, HRTEM images of (**e**) n = 2 phase in P10N0, (**f**) (110) in P6N4 and (**g**) (110) in mFP6N4.

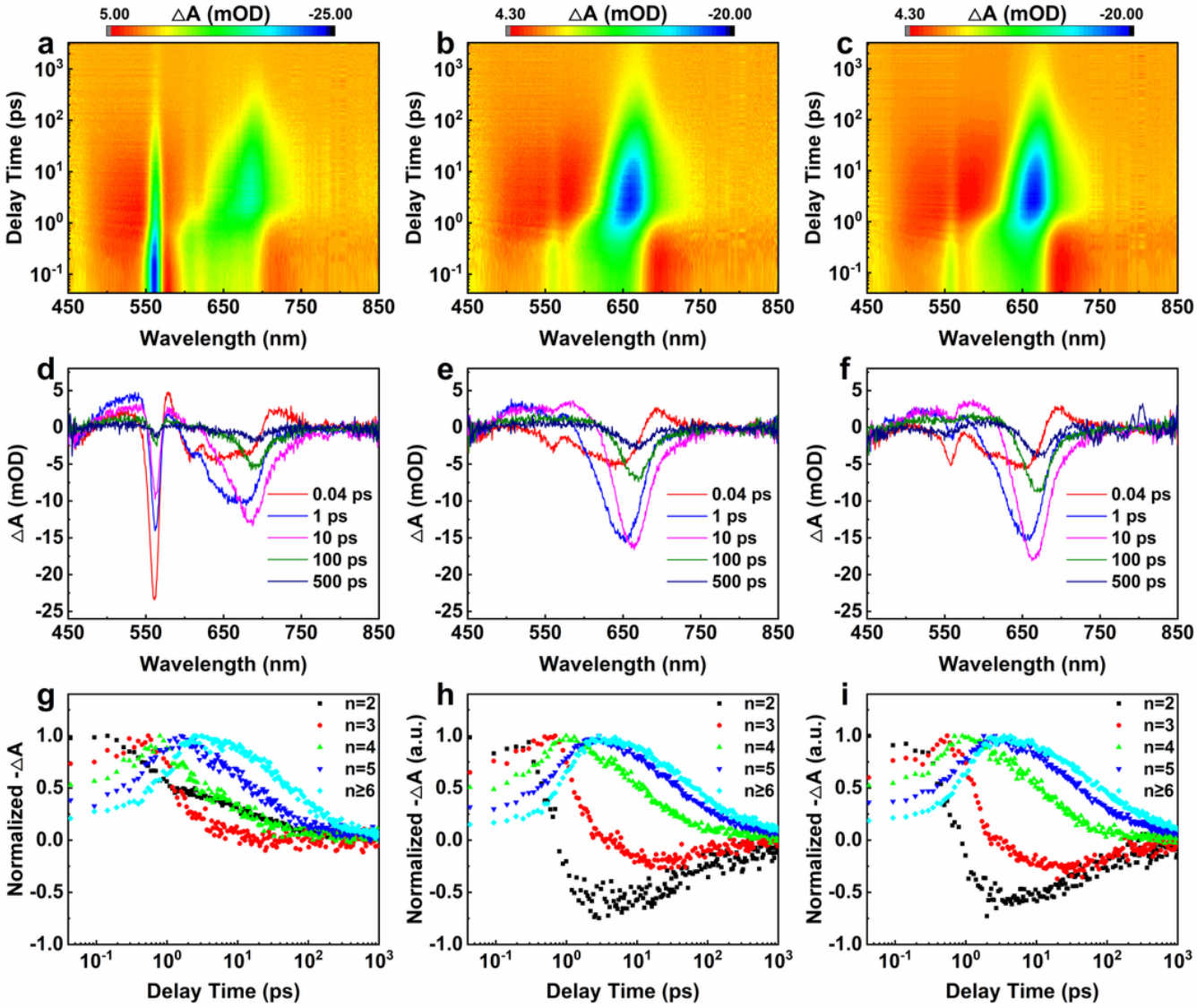

Figure 3

Transit absorption (TA) measurements of perovskite films. a-c, TA spectrum color map of (**a**) P10N0, (**b**) P6N4 and (**c**) mFP6N4. **d-f**, TA spectrum of (**d**) P10N0, (**e**) P6N4 and (**f**) mFP6N4 at different decay times. **g-i**, Decay kinetics about different phases of (**g**) P10N0, (**h**) P6N4 and (**i**) mFP6N4.

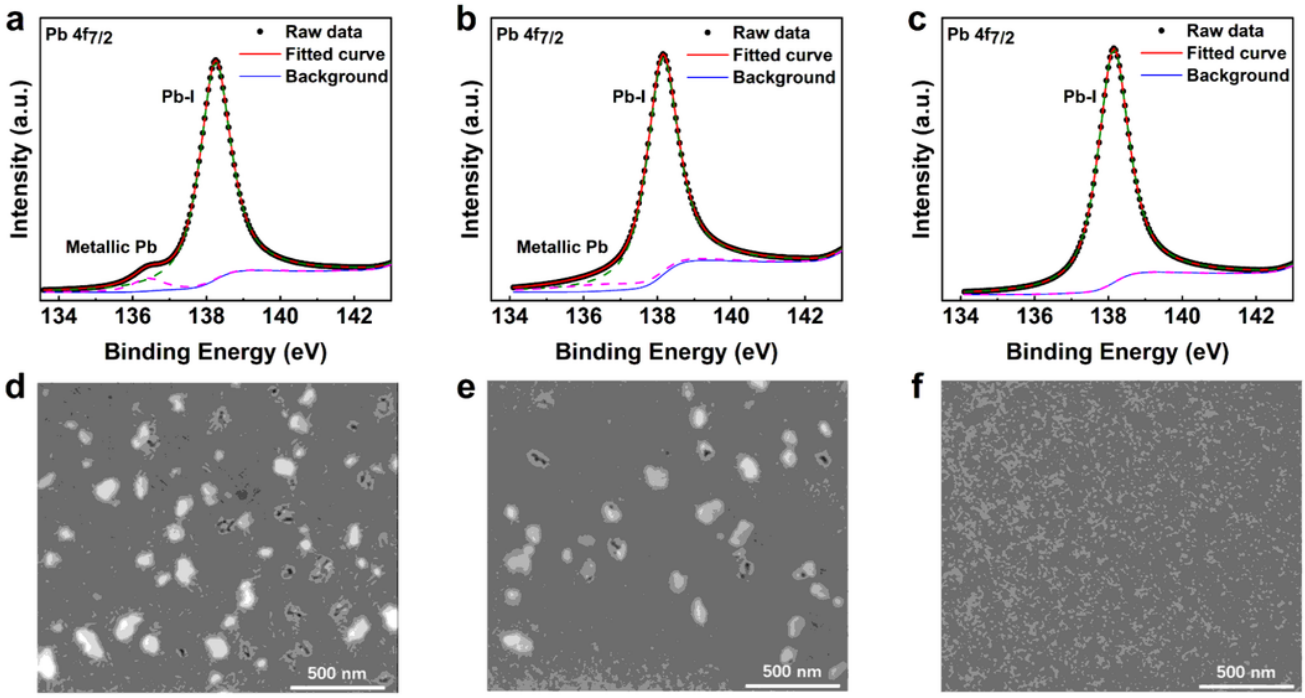

Figure 4

Chemical states and morphologies of perovskite films. **a-c**, Pb $4f_{7/2}$ core level spectra of X-ray photoelectron spectroscopy (XPS) from (**a**) P10N0, (**b**) P6N4 and (**c**) mFP6N4. **d-f**, Scanning electron microscopy (SEM) images of (**d**) P10N0, (**e**) P6N4 and (**f**) mFP6N4.

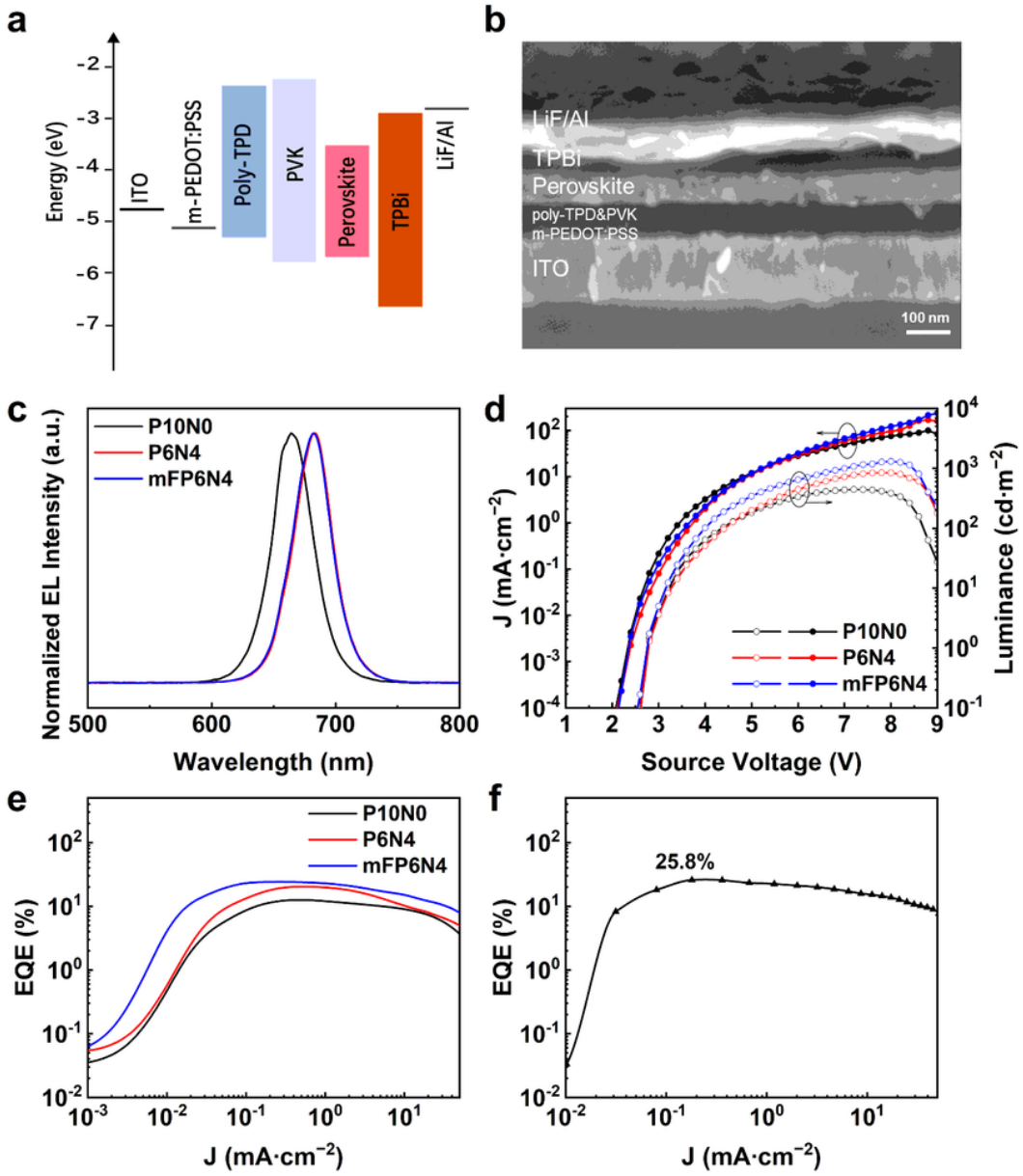

Figure 5

Characteristics of perovskite devices based on P10N0, P6N4, mFP6N4 films. **a**, Band energy level alignment for each layer of the PeLEDs devices. **b**, Cross-section Scan electron microscopy (SEM) image of perovskite devices. **c**, Normalized Electroluminescence (EL) spectra of PeLEDs with the different compositions of perovskite emitting. **d**, Current density-voltage-luminance characteristics of PeLEDs with the different compositions of perovskite emitting layer. **e**, EQE values versus current density of the PeLEDs with the different compositions of perovskite emitting layer. **f**, The EQE curve for the best performance of PeLED with 25.8% EQE.

Supplementary Files

This is a list of supplementary files associated with this preprint. Click to download.

- SupplementaryInformation.docx